https://doi.org/10.5194/egusphere-2026-3105
Preprint. Discussion started: 28 August 2026

Technical note: Comparison of Modeled Snow Permittivity and Density Estimates of Shallow, Wet Snowpacks using UAS-Lidar and UAS-GPR Observations

Minsun Kang[1,2], Adam Hunsaker[1,2], Mahsa Moradi[1,2], Dan R. Glaser[3], Jennifer M. Jacobs[1,2]

[1] Department of Civil and Environmental Engineering, University of New Hampshire, Durham, NH, USA
[2] Earth Systems Research Center, Institute for the Study of Earth, Oceans, and Space, University of New Hampshire, Durham, NH, USA
[3] Near-Surface Geophysics Group, US Army ERDC Cold Regions Research and Engineering Laboratory, Hanover, NH, USA

Correspondence to: Minsun Kang (MinSun.Kang@unh.edu)

Abstract. Seasonal snow density is a key determinant of snow water equivalent (SWE) and melt dynamics. However, characterizing its spatiotemporal variability is challenging, particularly in the shallow, ephemeral snowpacks of the eastern United States. This study evaluates the potential of integrating Ground Penetrating Radar (GPR) and LiDAR onboard an Uncrewed Aerial System (UAS) to assess the applicability of dielectric permittivity models for density retrieval in a transitional melt environment. Three field surveys were conducted at Kingman Farm, New Hampshire, where we collected UAS-GPR and in situ measurements of snow depth, density, and liquid water content (LWC) across open and sheltered fields between late February and early March, 2025. LiDAR-derived snow depth and GPR travel time were used to retrieve snow permittivity; these values were compared against theoretical estimates derived from seven dielectric models, including the physically-based Complex Refractive Index Model (CRIM) and six empirical formulations that account for snow wetness. Field observations revealed a rapid transition from dry to wet snow, with GPR-derived permittivity exhibiting a non-linear increase as LWC exceeded 3–4%. Comparisons showed that the physically based CRIM and the empirical Lundberg and Denoth models achieved comparably close agreement with GPR-derived permittivity (r = 0.70–0.71, RMSE ≈ 0.35). The remaining empirical models showed moderately larger error (RMSE = 0.40–0.48), while the Webb model showed weaker agreement (r = 0.54, RMSE = 0.79). These findings suggest that while empirical relationships performed reasonably well in transitional snowpacks outside the regions where they were established, applying physically-based models to UAS-GPR data offers an alternative and promising pathway for characterizing bulk snow properties in hydrologically complex environments.

https://doi.org/10.5194/egusphere-2026-3105
Preprint. Discussion started: 28 August 2026

1 Introduction

Snowpacks play a critical role in the Earth's water cycle, influencing land–atmosphere energy exchanges (Lehning, 2013; Thackeray et al., 2018) and the availability of water resources (Barnett et al., 2005; Hale et al., 2023). Snowpacks undergo accumulation, densification, and melt phases and have distinct properties that evolve throughout the winter season (Cheng et al., 2025; Judson & Doesken, 2000). In recent years, understanding and modeling hydrological processes has increasingly required observations of snow conditions across space and time (Jennings et al., 2018; Robinson et al., 1993).

Snow density is a fundamental physical property governing snowpack dynamics and evolution (Sturm et al., 2010) and is required, in combination with snow depth, to quantify snow water equivalent (SWE). It evolves continuously through snow metamorphism, that alters crystal size and shape, melt-refreeze cycles and compaction typically lead to progressive densification throughout the season (Pinzer and Schneebeli, 2009). Snow density exhibits significant spatial and temporal variability across different snowpack types and climate regions, which challenges the generalization of density information (Bormann et al., 2013; Zhao et al., 2023).

Measuring snow density using traditional in situ methods is destructive, labor-intensive, and yields sparse point observations that fail to capture the spatial heterogeneity of the snowpack. Recent studies have successfully derived snow density and SWE across space by using ground-based Ground Penetrating Radar (GPR) and exploiting the dependence of two-way travel time (TWT) on the relative dielectric permittivity of the snowpack (Bonnell et al., 2021; Mannello et al., 2025; McGrath et al., 2022). A powerful emerging approach is to combine ground-based GPR with Uncrewed Aerial Systems (UAS) lidar or photogrammetry observations of snow depth (Tan et al., 2017; Valence et al., 2022). Uncrewed Aerial Systems (UAS) provide a flexible and cost-effective platform for environmental data acquisition (Verfaillie et al., 2023; Whitehead et al., 2014). When instrumented with LiDAR or optical sensors, they can generate high-resolution maps (~ 1 m) of snow depth (Cho et al., 2025; Harder et al., 2020), enabling combine with other datasets. However, UAS snow depth does not directly constrain bulk density or liquid water content (LWC), limiting the ability to accurately estimate SWE or characterize the thermodynamic state of the snowpack. To address this limitation, Ground Penetrating Radar (GPR) is widely used as a complementary non-destructive technique to retrieve snowpack properties by analyzing the two-way travel time (TWT). One challenge to this approach is that interpreting a GPR signal response is often confounded by the complex dielectric influence of liquid water content (LWC).

Previous studies have successfully employed ground-based GPR to derive snow density and SWE by exploiting the dependence of TWT on the relative dielectric permittivity of the snowpack. To date, most GPR applications have focused on cold, deep, and predominantly dry snowpacks in alpine and high-latitude environments (Bonnell et al., 2023; Bradford et al., 2009; McGrath et al., 2022; Webb et al., 2018; Wilhelms, 2005). In these settings, LWC is negligible, and snow permittivity can be reasonably approximated as a two-phase mixture of ice and air. Consequently, inversion approaches developed for such conditions implicitly assume a relatively simple and temporally stable electromagnetic regime, where permittivity variations primarily reflect changes in density.

In contrast, shallow and wet snowpacks, common in transitional and ephemeral snow regions, depart fundamentally from these assumptions. Even small volumetric fractions of liquid water substantially increase bulk permittivity because the dielectric constant of water is an order of magnitude larger than that of ice or air (Tiuri et al., 1984). This introduces strong nonlinearity in the relationship between TWT, density, and LWC, as well as

https://doi.org/10.5194/egusphere-2026-3105
Preprint. Discussion started: 28 August 2026

increased attenuation and signal dispersion. To account for the influence of liquid water, several empirical and semi-empirical formulations have been proposed (Kendra et al., 1994; Lundberg and Thunehed, 2000; Tiuri et al., 1984; Webb et al., 2021). However, these parameterizations were derived under controlled laboratory settings or site-specific field conditions, typically for deeper, seasonal snowpacks. They have rarely been evaluated in shallow, spatially heterogeneous, and dynamically wet snowpacks, and their reliability is not well constrained. The transferability of fitted coefficients across different snow climates or melt stages remains unknown.

A potential alternative to current empirical relationships is the Complex Refractive Index Model (CRIM), a physically based dielectric mixing formulation derived from the general Lichtenecker–Rother expression (Simpkin, 2010). CRIM estimates effective permittivity as a volumetric mixture of constituent phases without requiring snow-specific calibration parameters. The model has been widely applied in consolidated and unconsolidated porous materials where air, solid, and liquid phases coexist within heterogeneous pore structures (Ajo-Franklin et al., 2004; Arcone & Boitnott, 2012; Glaser et al., 2012; Endres and Knight, 1992; Glaser et al., 2022b). Yet, despite its extensive use in other multiphase porous media, CRIM has not been evaluated for snowpacks, particularly not for shallow, wet snow typical of temperate regions such as the eastern United States. Snowpacks represent a highly porous, multiphase medium analogous to partially saturated soils, where air, ice (solid), and liquid water coexist within a dynamic evolving pore structure (Artemov, 2019; Garcia and Glaser, 2025). Assessing the applicability of a physically based mixing model in this underrepresented snow regime therefore represents a critical step toward extending GPR-based SWE estimation beyond the cold, dry conditions that have dominated prior research.

Given these complexities and limitations of prior studies, this study investigates the feasibility of UAS-LiDAR snow depth and UAS-GPR to acquire spatially distributed snowpack depth and TWT and derive relative dielectric permittivity in shallow, wet snow conditions. The specific objectives of this work are to: 1) characterize the spatiotemporal variability of snow depth, density, and LWC based on in situ measurements; 2) assess the relationship between GPR-derived permittivity and in situ snow properties; and 3) evaluate the applicability of empirical and physical models for retrieving snow density in shallow, wet seasonal snowpacks. The study also presents a novel non-destructive, Federal Communications Commission (FCC) compliant UAS platform for collecting co-located GPR TWT and the LiDAR-derived snow depth measurements.

2 Study Area

In situ measurements were conducted at Kingman Research Farm in Durham, New Hampshire, USA (43.168–43.177°N, 70.920–70.935°W; Fig. 1). The study area encompasses approximately 360 acres of mixed agricultural and forested areas. The study area lies within a transitional snow regime (Johnston et al., 2024), an intermediate class between persistent seasonal snow and short-lived ephemeral snow, characterized by shallow, wet, and highly variable snow cover with frequent midwinter melt events and repeated snow on–off cycles. This study specifically focused on two contrasting site conditions to evaluate UAS-GPR performance under varying microclimate and snowpack conditions: an open pasture field (OP) and a sheltered field (SF). OP is a largely exposed pasture characterized by high solar radiation, bounded by a mixed deciduous-coniferous forest to the north. In contrast, SF is a smaller, forest-sheltered field with reduced solar exposure, surrounded by tall coniferous and deciduous

https://doi.org/10.5194/egusphere-2026-3105
Preprint. Discussion started: 28 August 2026

trees. The forest canopy attenuates direct solar irradiance and reduces wind exposure, resulting in a more shaded and sheltered environment compared to OP.

During the UAS-GPR observation period from January to March 2025, the study site experienced a clear seasonal transition in hydrometeorological conditions (Fig. S1). Daily air temperatures remained predominantly below 0°C through January and mid-February, followed by a warming trend beginning in late February. This transition coincided with a pronounced increase in incoming solar radiation, reflecting seasonal progression and increasing solar elevation angles toward early spring. Several precipitation events occurred throughout the period. Notably, precipitation during the interval between the first (Feb. 25) and second (Mar. 4) UAS surveys consisted exclusively of snowfall, whereas events between the second and third (Mar. 9) surveys consisted primarily of mixed-phase precipitation, reflecting a transition from snow to rain.

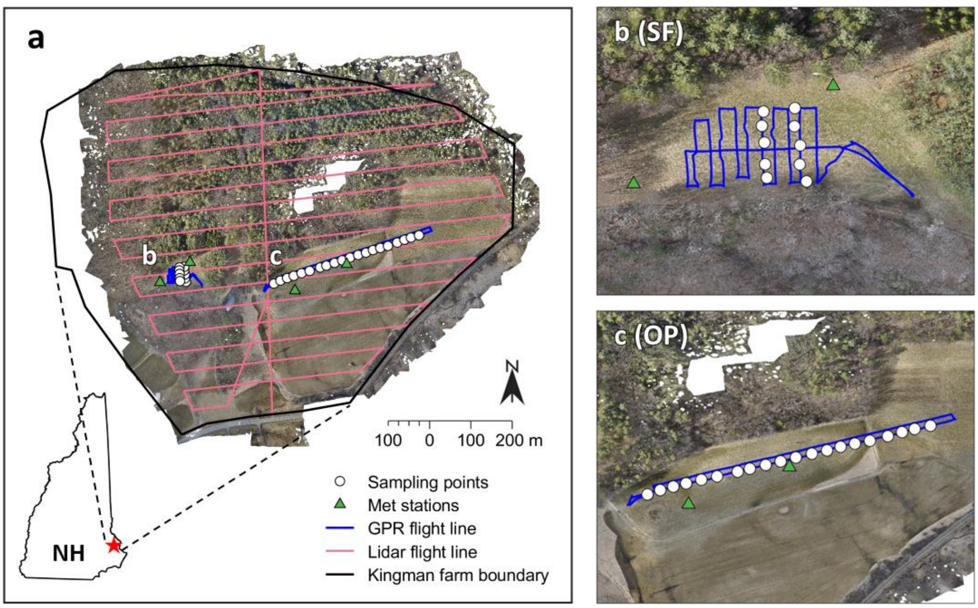

Figure 1: (a) Map of the Kingman Farm study area in Durham, New Hampshire, illustrating UAS-GPR and LiDAR flight lines and locations of in situ measurements. The study area comprises two distinct field types: (b) a sheltered field (SF; top right) and (c) an open pasture field (OP; bottom right).

3 Materials & Methods

3.1 In situ measurements

Three UAS-GPR surveys were conducted concurrently with in situ snow measurements on February 25, March 4, and March 9, 2025. Measurements were taken at 30 spatially distributed points (20 in the OP and 10 in the SF) during each survey date at 10 m intervals. Snow depth was measured at each point using a snow probe, and bulk density was obtained from nearby snow pits by weighing snow samples on a field scale. LWC was measured with a Snow Fork, with three repeated readings per point to ensure data reliability; the average value was used for analysis.

https://doi.org/10.5194/egusphere-2026-3105
Preprint. Discussion started: 28 August 2026

3.2 Uncrewed Aerial System (UAS) observations

3.2.1 Ground Penetrating Radar (GPR) measurements and processing

A pulsed GPR antenna and control unit were mounted on a heavy-lift DJI Matrice 600 Pro for UAS operation. The GSSI Inc. GPR system was comprised of a shielded monostatic 900 MHz antenna and a SIR-4000 control unit (used to define radar parameters and log the observations). Each radar pulse was configured to be sampled 512 times over a duration of 40 ns. This sampling duration allowed the radar wave to propagate through the shallow snowpack and into the underlying soil, with 512 samples being sufficient to resolve the respective snow–air and snow–ground horizons while maintaining a high spatial density (~1 GPR scan per cm).
Real-Time Kinematic (RTK)–corrected positions, needed for accurate georeferencing of GPR scans, were obtained from an Emlid M2 GNSS receiver mounted on the UAS platform. An Emlid RS2+ was used as a stationary base station, with corrections being sent to the UAS receiver over a radio link. RTK-corrected positions of the UAS platform were sampled at a frequency of 5 Hz and streamed to the SIR-4000 over a serial cable for georeferencing GPR observations. Considering the UAS flight speed (2 m/s), GPR traces per second (177 traces/s), and the position sampling rate (5 Hz), two sampled positions were obtained per meter along the flight path. Coordinates of each trace were then obtained by interpolation.
To satisfy FCC regulations limiting air-coupled GPR to close proximity to the ground, a true terrain module was integrated into the UAS platform. The true terrain module was provided by SPH Engineering and uses a laser altimeter to continuously monitor flight altitude and automatically adjust the flight controls to maintain a user-defined altitude. An altitude of 1 m was used here to comply with regulations and to limit radar attenuation through the air.
Several post-processing steps were applied to improve interpretation of the GPR radargrams. Data collected during takeoff and landing were first removed, followed by truncation of the first 100 samples of each trace to eliminate direct reflections and air-path returns. Background removal and adaptive gain were then applied to suppress static noise and enhance reflections. Deconvolution was used to mitigate banding artifacts caused by repeated and delayed reflections of the same horizons. Finally, a semi-automated picking algorithm was used to identify the snow–air and snow–ground horizons, enabling calculation of TWT used to derive snow properties.
The relative permittivity (ε) of the snowpack was calculated by integrating GPR TWT measurements with the co-located LiDAR-derived snow depth (details in Section 3.2.2). First, the effective radar propagation velocity (v) within the snow layer was calculated as:

$$v = \frac{2 \times d_{LiDAR}}{T} \quad (1)$$

where d_{LiDAR} is the snow depth obtained from the processed LiDAR and T is the two-way travel time (TWT) of the radar signal reflected from the snow–ground interface. Using the calculated velocity, the relative dielectric permittivity was subsequently derived from the electromagnetic wave propagation relationship:

$$\varepsilon = \left(\frac{c}{v}\right)^2 \quad (2)$$

where c is the speed of light in a vacuum (≈0.3 m/ns). The resulting relative permittivity represents the vertically averaged dielectric property of the snowpack and is subsequently compared against in situ measurements and permittivity values modeled from in situ density and LWC.

https://doi.org/10.5194/egusphere-2026-3105
Preprint. Discussion started: 28 August 2026

More generally, the electromagnetic behavior of snow is described by a complex permittivity ($\varepsilon *$), which accounts for both energy storage and energy loss within the medium (von Hippel and Morgan, 1955) . In phasor form this can be written as:

$$\varepsilon *= \varepsilon' - i\varepsilon'' \quad (3)$$

where ε' is the real permittivity, which governs energy storage and wave propagation velocity, and ε'' is the imaginary permittivity, which represents dielectric loss. The ratio of these components is commonly expressed as the loss tangent, tan $\delta = \varepsilon''/\varepsilon'$.

In conductive and multiphase media, the imaginary component includes a contribution from electrical conductivity, such that:

$$\varepsilon *= \varepsilon' - i\left(\varepsilon''_d + \frac{\sigma}{\omega\varepsilon_0}\right) \quad (4)$$

where ε''_d represents the dielectric loss, σ is the conductivity, ω is the angular frequency, and ε_0 is the permittivity of free space. Thus, bulk electromagnetic behavior depends not only on phase-dependent dielectric storage, but also on dissipative processes associated with liquid water content, phase connectivity, and electrical conduction (Schön, 2015). Because the permittivity estimated in this study is derived from radar wave velocity using two-way travel time, the resulting values primarily reflect the real component of the bulk electromagnetic response.

The relative contributions of dielectric storage and conductive loss are frequency dependent. As noted above, all GPR measurements in this study were acquired using a 900 MHz antenna; therefore, the permittivity values reported here represent the effective dielectric response at this frequency. As a result, the inferred bulk properties reflect frequency-specific electromagnetic behavior and may differ from those observed at lower or higher frequencies. Additionally, these measurements represent instantaneous conditions along each radar transect, implicitly assuming that temporal changes in pore structure, phase distribution, and temperature are negligible over the acquisition period, while spatial variability is resolved within the radargrams.

3.2.2 LiDAR measurements and processing

High-resolution snow depth observations were acquired using a UAS LiDAR platform following each UAS-GPR survey. The LiDAR payload used here was the Phoenix miniRanger3-lite. This payload integrates the RIEGL miniVUX-3 laser scanner and the NovAtel OEM7 INS. Horizontal and vertical accuracies were assessed for each LiDAR survey using five ground control points (GCPs) placed throughout the survey area. Each GCP was surveyed using an Emlid RS3, obtaining RTK corrections from an on-site GNSS base station (Emlid RS2+). Horizontal accuracies were within ±1 cm, and vertical accuracies were within ±2.5 cm. For each survey, a double-grid flight pattern was flown at an altitude of 100 m and a flight speed of 7 m/s.

Post-processing of the acquired UAS LiDAR data was performed using the SpatialExplorer 9.0.1 software package provided by Phoenix LiDAR Systems. The trajectory of each UAS survey was differentially corrected using GNSS observables collected by the on-site base station. Automatic boresighting and trajectory optimization routines were applied to ensure accurate sensor alignment and reduce processing artifacts. Ground points were identified using an implementation of the Progressive TIN Densification algorithm and subsequently gridded at a

https://doi.org/10.5194/egusphere-2026-3105
Preprint. Discussion started: 28 August 2026

50 cm resolution. Snow depth maps were then generated by differencing snow-on and snow-free digital elevation models (DEMs). Bilinear interpolation resampling was used to align the snow-free and snow-on grids prior to differencing. This was done in an effort to reduce alignment artifacts resulting from resampling.

3.3 Permittivity models

To quantitatively evaluate the performance of the UAS-GPR system, the retrieved radar-derived permittivity were compared against six dielectric permittivity models using in situ measurements (snow density and LWC) (Mitterer et al., 2011; Webb et al., 2021). Only permittivity (ε) models that include the effect of both LWC (θ_w) and snow density (ρ_s) were considered. Specifically, we evaluated empirical relationships derived by (Denoth, 1997; Kendra et al., 1994; Lundberg and Thunehed, 2000; Sihvola and Tiuri, 1986; Webb et al., 2021), alongside the relationship used by A2 Photonic Sensors (2019) (Table 1). These empirical models were assessed together with the physically based CRIM to determine the suitability of existing parameterizations for characterizing shallow, wet snowpacks in our study region.

Empirical relationships are commonly used to relate the dielectric constant of snow to its physical parameters, such as density and LWC. Sihvola and Tiuri (1986) provided a model where the real part of snow permittivity is a function of dry snow density and volumetric water content at 1 GHz. Similarly, Denoth (1997) developed a simple monopole-antenna probe to measure LWC in snow and soils in situ by inverting the antenna input impedance over a 0.2–2 GHz frequency range to retrieve the effective permittivity of the surrounding medium. Kendra et al. (1994) developed a coaxial cavity snow probe that measures the complex dielectric constant in situ and derived semi-empirical relationships to retrieve LWC and snow density with improved accuracy. Lundberg and Thunehed (2000) showed that an LWC of about 5% changes the empirical coefficient used to convert radar travel time to SWE by approximately 20% compared to dry snow. Recent evaluations by Webb et al. (2021) addressed the applicability of these classic models for low-frequency radar and proposed revised empirical coefficients for dry and wet seasonal snowpacks.

https://doi.org/10.5194/egusphere-2026-3105
Preprint. Discussion started: 28 August 2026

Table 1: Summary of permittivity models evaluated in this study. Each equation represents the relationship between permittivity (ε), density (ρ_s, kg/m^3), and liquid water content (θ_w, cm^3/cm^3).

Model	Equation for permittivity	Reference
Sihvola	$\varepsilon = 1 + 1.7\left(\frac{\rho_s}{1000} - \theta_w\right) + 0.7\left(\frac{\rho_s}{1000} - \theta_w\right)^2 + 8.7\theta_w + 0.007(100\theta_w)^2$	Sihvola & Tiuri (1986)
Kendra	$\varepsilon = 1 + 1.7\left(\frac{\rho_s}{1000} - \theta_w\right) + 0.7\left(\frac{\rho_s}{1000} - \theta_w\right)^2 + \Delta,$ $\Delta = 0.02(100\theta_w)^{1.015} + [0.073(100\theta_w)^{1.31}]/1.0122$	Kendra et al. (1994)
Lundberg	$\varepsilon = \left(1 + 0.851\frac{\rho_s}{1000} + 7.093\theta_w\right)^2$	Lundberg & Thunehed (2000)
Denoth	$\varepsilon = 1 + 1.92\left(\frac{\rho_s}{1000}\right) + 0.44\left(\frac{\rho_s}{1000}\right)^2 + 18.7\theta_w + 45\theta_w{}^2$	Denoth (1997)
Webb	$\varepsilon = [1 + 0.0014(\rho_s - 1000\theta_w) + 2\times10^{-7}(\rho_s - 1000\theta_w)^2] + \left(0.01\theta_w + 0.4\theta_w{}^2\right)\varepsilon_w,$ $\varepsilon_w = 87.9$	Webb et al. (2021)
A2	$\varepsilon = 1 + 1.202\left(\frac{\rho_s}{1000} - \theta_w\right) + 0.983\left(\frac{\rho_s}{1000} - \theta_w\right)^2 + 21.3\theta_w$	A2 Photonic Sensors (2019)

https://doi.org/10.5194/egusphere-2026-3105
Preprint. Discussion started: 28 August 2026

The CRIM is implemented in this study as a physically based dielectric mixing model for estimating the effective permittivity of snow. In the generalized Lichtenecker-Rother form, the effective permittivity is written as:

$$\varepsilon_{\mathrm{eff}}^{\alpha} = V_a \varepsilon_a^{\alpha} + V_i \varepsilon_i^{\alpha} + V_w \varepsilon_w^{\alpha} \tag{5}$$

where V_a, V_i, and V_w are the volume fractions of air, ice, and liquid water, ε_a, ε_i, and ε_w are their corresponding dielectric permittivities, and α is a dimensionless exponent that reflects bulk geometric and connectivity effects. Setting $\alpha = 0.5$ reduces this expression to the CRIM formulation,

$$\sqrt{\varepsilon_{\mathrm{eff}}} = V_a \sqrt{\varepsilon_a} + V_i \sqrt{\varepsilon_i} + V_w \sqrt{\varepsilon_w} \tag{6}$$

which corresponds to an effectively isotropic medium (Simpkin, 2010).

Previous comparisons of dielectric mixing laws show that fixing $\alpha = 0.5$ provides stable estimates of effective permittivity across broad phase proportions and avoids the nonuniqueness that can occur when α is treated as a free parameter (Simpkin, 2010). Under conditions where pore geometry and phase connectivity are not independently constrained, CRIM performs as well as or better than alternative formulations, including parallel, series, cubic, and unmodified Lichtenecker-Rother mixing laws (Ajo-Franklin et al., 2004; Glaser et al., 2012, 2022a; Leão et al., 2015).

Modified Lichtenecker-Rother formulations can outperform CRIM in controlled laboratory settings when additional geometric weighting terms and end-member measurements are available (Glaser et al., 2022a). However, such detailed constraints are not available in the UAS-GPR dataset. Under these conditions, CRIM provides a physically consistent and practically implementable framework for relating bulk permittivity to phase volumetric fractions. Accordingly, CRIM is adopted here as the primary theoretical model for linking GPR-derived permittivity with snow density and LWC.

4 Results and Discussion

4.1 Field observations of snow depth, density, and wetness

The three field surveys were conducted after peak snow from the end of February to early March. The period had a range of temperature and solar radiation conditions that resulted in intermittent freezing and thawing conditions (Fig. S1). Precipitation during the interval between the first and second surveys consisted exclusively of snowfall, whereas the period between the second and third surveys was characterized by mixed-phase precipitation which transitioned from snow to rain.

Figures 2 and 3 show in situ measurements of snow depth, density, and LWC along the OP (20 points) and SF (10 points) transects, respectively, for the three survey dates (25 February, 4 March, and 9 March 2025). On February 25$^{\text{th}}$, snow conditions were relatively dry and the snowpack depth and density were fairly consistent at both locations. The mean snow depth was 31.8 ± 2.3 cm in the OP and 38.3 ± 1.4 cm in the SF, with no spatial gradients evident along either transect. Snow density was relatively low for both transects (0.25 ± 0.03 g/cm^3 at OP and 0.28 ± 0.03 g/cm^3 at SF), and LWC was below 2% at most sampling points.

By March 4$^{\text{th}}$, differences between the OP and SF transects had emerged. At the OP, mean snow depth decreased from 31.8 cm to 20.7 cm (± 2.3), while the mean density increased to 0.40 g/cm^3 (± 0.05) and the LWC ranged from 0.3 to 3.6%. At the SF, snow depth had also decreased by about 10 cm (27.6 ± 3.8 cm), with greater spatial

https://doi.org/10.5194/egusphere-2026-3105
Preprint. Discussion started: 28 August 2026

variability. The increase in mean density to 0.37 g/cm^3 was similar to the OP. LWC showed a south-to-north gradient, with lower values at the south of the transect and higher values toward the north, and a mean of 2.65%. Between the March 4th and March 9th flights, temperatures increased to above freezing and there was 7.7 cm of rain. On March 9th, the OP had a shallow (7.6 cm), wet (4.3%), and dense (0.42 g/cm^3) snowpack with favorable conditions for melting. The SF retained more snow with a mean depth of 16.5 cm, but a comparable density (0.40 g/cm^3). However, the OP site had a broader density range due to prolonged exposure leading to greater compaction in some areas. In contrast, the SF site showed a more stable density distribution. Across all dates, relative depth patterns along each transect were consistent (i.e., locations that were initially deeper tended to remain deeper).

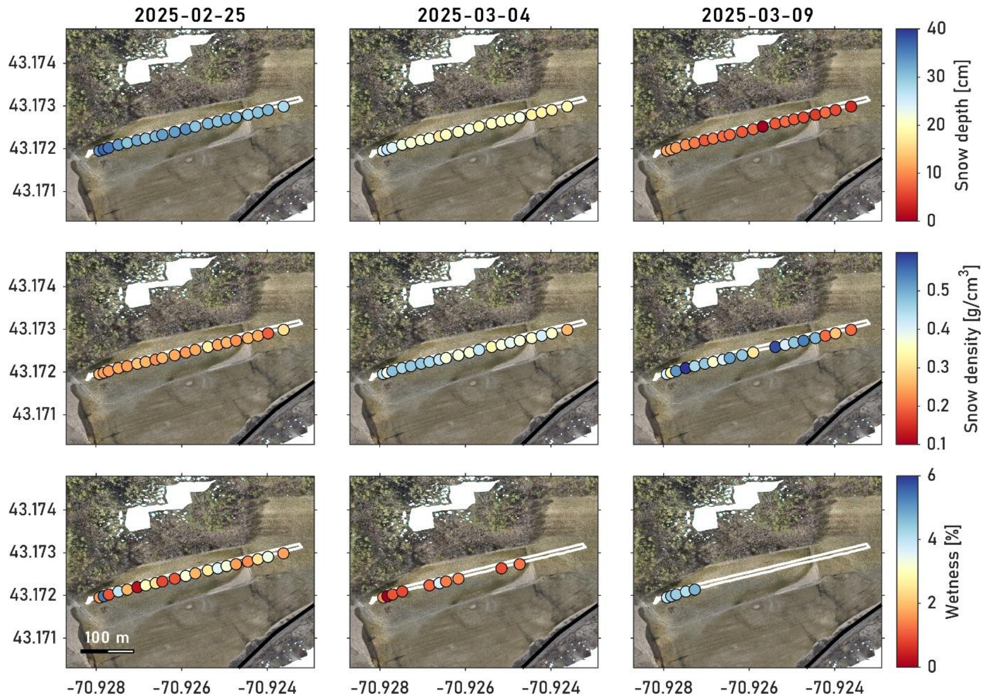

Figure 2: Spatial distribution of snow depth, snow density, and snow wetness (liquid water content; LWC) measured at Kingman Farm (OP) on February 25th, March 4th, and March 9th 2025.

https://doi.org/10.5194/egusphere-2026-3105
Preprint. Discussion started: 28 August 2026

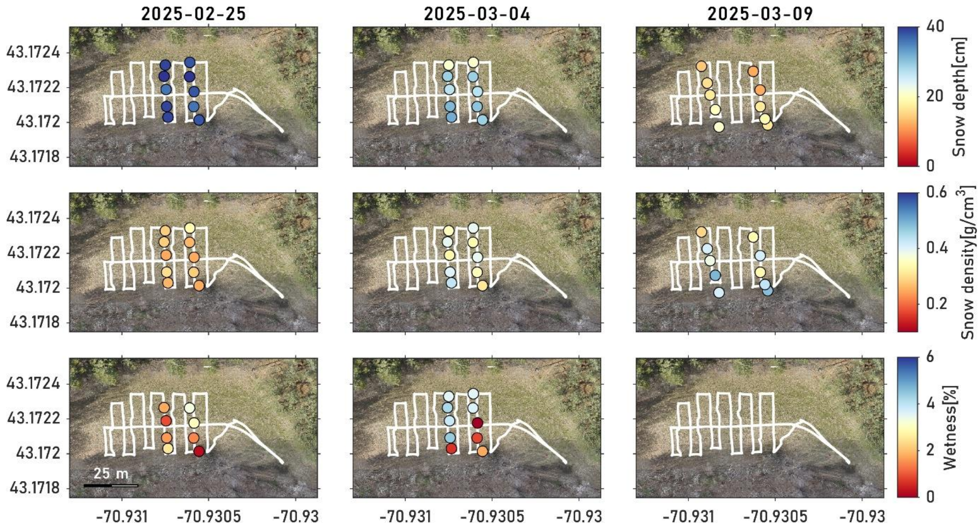

Figure 3: Spatial distribution of snow depth, snow density, and snow wetness (LWC) measured at Kingman Farm (SF) on February 25th, March 4th, and March 9th 2025.

4.2 Relationships between permittivity and snow properties

Figure 4 shows the relationships between GPR-derived dielectric permittivity and in situ snow properties measured at Kingman Farm. Permittivity generally decreased with increasing snow depth, indicating that shallower snowpacks had higher dielectric responses, particularly during the early-March melt at OP. In contrast, a positive relationship was observed between permittivity, snow density, and LWC. This pattern was consistent across both fields and survey periods, suggesting that snow density and LWC were the primary drivers of dielectric variability under open and sheltered conditions. The relationship between permittivity and LWC was nearly constant for LWC below 2%, whereas it increased sharply when LWC exceeded 3–4%, reflecting the transition from dry to wet snow. This nonlinear increase in permittivity with increasing liquid water content is consistent with volumetric mixing behavior observed in other partially saturated porous media, where small increases in conductive fluid fraction disproportionately influence bulk electromagnetic properties (Garcia and Glaser, 2025; Glaser et al., 2022b; Glaser et al., 2023). As described in Section 3.2.1, the permittivity derived from travel-time measurements primarily reflects the real component of the snowpack's complex dielectric response; however, increasing liquid water content may also enhance conductive pathways and associated loss mechanisms, contributing to the imaginary component of permittivity and, in turn, to increased signal attenuation.

The three survey dates showed distinct dielectric values, corresponding to snow conditions that evolved from relatively dry to increasingly wet conditions (Fig. S1). On February 25th, the low permittivity values were consistent with a relatively dry snowpack. Although daily mean air temperature reached about +5 °C on February 25th, freezing conditions (< 0 °C) persisted before that date, increasing the energy needed for ripening and melting. Therefore, the snowpack measured on February 25th was likely dry, as the short warming phase was insufficient

https://doi.org/10.5194/egusphere-2026-3105
Preprint. Discussion started: 28 August 2026

to initiate liquid water formation within the snow layer. By March 4th, daily air temperatures had risen to near 0 °C, accompanied by an increase in solar radiation, which initiated partial surface melting and led to slightly higher permittivity in the shallower snow. On March 9th, when the mean air temperature exceeded 5 °C and additional precipitation had occurred, LWC increased to 4–5%, producing a rapid rise in permittivity (around 4). Consequently, permittivity decreased with increasing snow depth, indicating that the shallow snowpacks became wetter while the deeper ones remained relatively cold and dry.

https://doi.org/10.5194/egusphere-2026-3105
Preprint. Discussion started: 28 August 2026

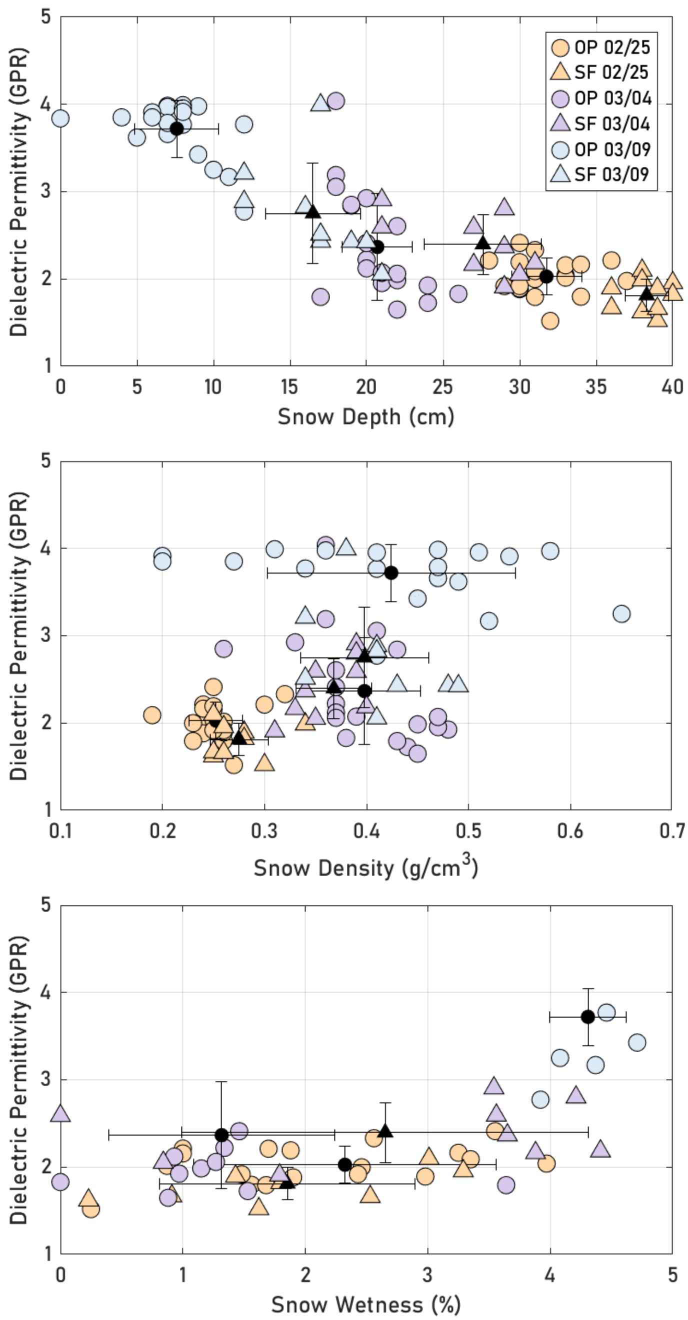

310 **Figure 4: Relationships between GPR-derived permittivity and snow properties (snow depth, density, and wetness) measured at Kingman Farm. Each colored symbol represents an individual observation from OP and SF with colors**

https://doi.org/10.5194/egusphere-2026-3105
Preprint. Discussion started: 28 August 2026

reflecting the survey date. Black symbols indicate the mean values for each site/date group, with horizontal and vertical error bars showing one standard deviation of the x- and y-variables, respectively.

4.3 Comparison of Permittivity Models

Figure 5 compares GPR-derived permittivity values with those estimated from the six empirical models and the physically based model (CRIM). Across all models, the correlation coefficients ranged from 0.54 to 0.71, and the root mean square errors (RMSE) from 0.35 to 0.79, indicating moderate to strong linear relationships with model-dependent bias patterns. Among the empirical models, the Lundberg (r = 0.71, RMSE = 0.35) and Denoth (r = 0.70, RMSE = 0.35) models performed best, followed by A2 and Kendra. The Sihvola model exhibited slightly larger deviations, particularly at higher permittivity. The Webb model yielded markedly lower agreement (r = 0.54, RMSE = 0.79), underestimating permittivity for wet-snow conditions. The CRIM model (r = 0.71, RMSE = 0.35) performed well relative to the empirical models across the full range of observed permittivity, showing minimal bias over dry and wet conditions. These results suggest that, although all models reproduced the general trend of GPR permittivity, their accuracy varies depending on their formulation and calibration environment.

The performance differences among models in Fig. 5 can be explained by their structural assumptions and calibration ranges. The Sihvola model tends to underestimate permittivity relative to GPR measurements, likely because its original calibration was limited to dry or slightly wet snow (LWC ≤ 0.05), making it less representative of the transitional wetness observed in this study. The Denoth model, originally developed for Alpine snow with densities of 0.48–0.58 g/cm^3, reproduced most field conditions well, but also underestimated permittivity under wetter, high-density conditions observed on March 9th at the OP. The Webb model underestimated permittivity, which likely reflects the model's empirical calibration under isothermal wet-snow conditions with permittivity of 1.15–2.83. These conditions differed from the transitional and partially wet snow conditions observed at Kingman Farm. Webb et al. (2021)'s finding that their model behaves similarly to the Sihvola model under lower LWC agrees with this study's results. In contrast, the Lundberg formulation, based on a three-phase dielectric mixing approach (air–ice–water), performed comparably to CRIM, as both capture the increase in permittivity with LWC through volumetric mixing of snow.

The CRIM model reproduced the GPR-derived permittivity well across both dry and wet snow conditions. Unlike the empirical models, CRIM calculates bulk permittivity from the volumetric fractions. In this study, CRIM assumes that the snowpack behaves as a three-phase medium in which air, ice, and water are the volumetric components. This physically based structure allows the model to adapt to variations in snow density and LWC without site-specific calibration. Furthermore, CRIM's square-root dependence on phase fractions was able to capture our field data's nonlinear relationship between permittivity and LWC (Fig. 4), enabling a realistic representation of the observed snow conditions.

https://doi.org/10.5194/egusphere-2026-3105
Preprint. Discussion started: 28 August 2026

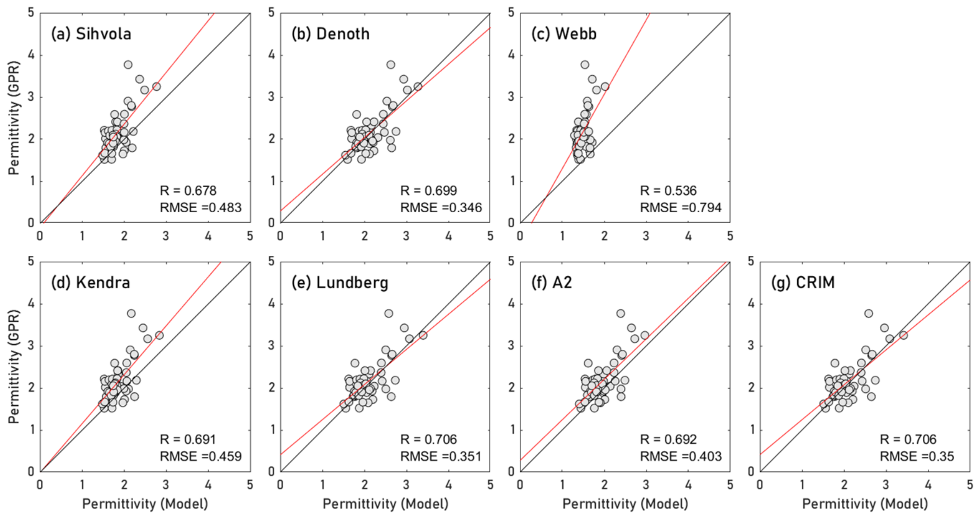

Figure 5: Comparison between GPR-derived permittivity and modeled permittivity from seven permittivity models: (a) Sihvola and Tiuri (1986), (b) Denoth (1997), (c) Webb et al. (2021), (d) Kendra et al. (1994), (e) Lundberg & Thunehed (2000), (f) A2 Photonic Sensors, and (g) complex refractive index model (CRIM). The black line indicates the 1:1 reference, and the red line shows the regression line.

4.4 CRIM Modeled relationships between permittivity, density, and wetness

To examine whether our observed combinations of permittivity, density, and liquid water content reflect physically reasonable snow wetness states, we compared the field measurements with CRIM-modeled curves for snow densities ranging from 0.1 to 0.7 g/cm^3 (Fig. 6). Figure 6 highlights two important aspects of the CRIM model. First, the CRIM model curves exhibit physically consistent behavior. Bulk permittivity increases monotonically as volumetric liquid water content increases and, for a given water fraction, increases with snow density. Second, the observations closely align with the CRIM modeled values, with only a few observations deviating from the modeled range. For example, the March 9th OP observation, LWC $\approx$ 5% and GPR-derived permittivity $\approx$ 3.7, had a field density that was less than half CRIM's modeled density. Mapped density differences (Figure S2) show that this location's in-situ density was lower than that observed at surrounding locations. The shallow depths on this date likely made it difficult to obtain highly accurate density measurements using a snow tube.

https://doi.org/10.5194/egusphere-2026-3105
Preprint. Discussion started: 28 August 2026

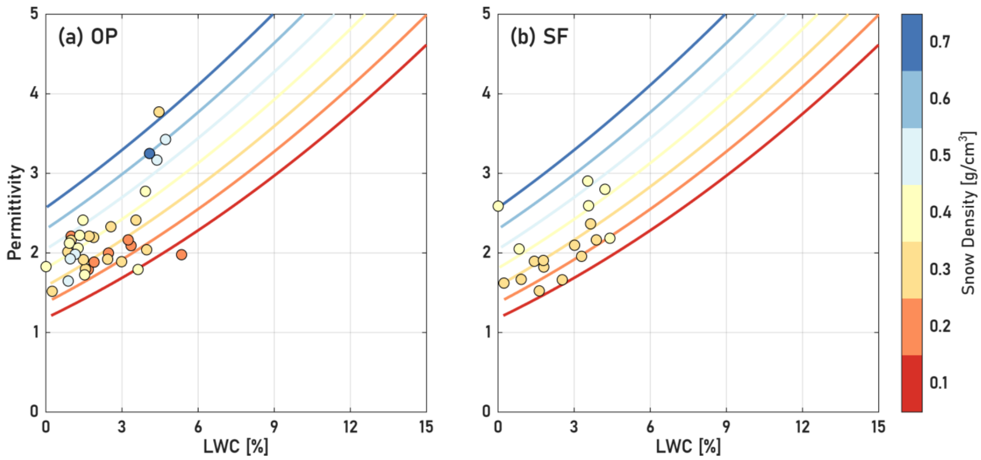

Figure 6: Relationship between permittivity, LWC, and snow density for OP and SF sites. Solid lines represent CRIM-derived curves for densities ranging from 0.1 to 0.7 g/cm^3, and circles indicate in situ measurements.

The relationship between in situ snow density and CRIM-derived density exhibited differences across the two distinct transects (Fig. 7). At the OP, the data points showed a weaker linear correlation across a wider range of density (r = 0.43, RMSE = 0.14 g/cm^3), while the SF were more clustered and consistent points (r = 0.61, RMSE = 0.12 g/cm^3). The density differences in OP were pronounced when LWC exceeded 4%. This pattern is consistent with observations from Bonnell et al. (2021), who showed that radar velocity is more sensitive to LWC than to density, especially when preferential flowpaths create high heterogeneity. Under these conditions, bulk LWC measurements fail to capture the non-uniform water distribution within the snowpack. Consequently, this discrepancy may have caused CRIM-derived estimates to diverge from in situ measurements as LWC increases, particularly in the more exposed open environment. In contrast, the SF exhibited higher consistency, which can be attributed to the influence of the forest canopy. According to Roth and Nolin (2017), canopy cover substantially reduces wind speeds and suppresses turbulent fluxes, contributing to a more stable snowpack. This sheltered environment maintains a less variable snow structure, allowing more reliable density estimates at the SF site. In this site, the CRIM model overestimated the range of density values compared to the observed densities.

https://doi.org/10.5194/egusphere-2026-3105
Preprint. Discussion started: 28 August 2026

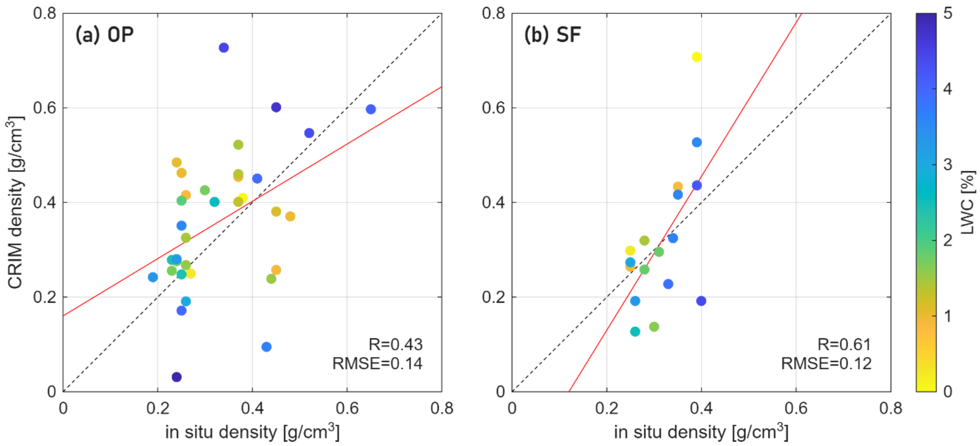

Figure 7: Comparison between CRIM-derived snow density and in situ measured density at (a) OP and (b) SF sites.

5 Summary and Conclusion

This study evaluated the dielectric characteristics of shallow, wet snowpacks measured on three dates in two different field environments using co-located GPR TWT and the LiDAR-derived snow depth observations from a novel non-destructive, FCC compliant UAS platform. Over the three survey dates, mean snow depth decreased from about 32 to 8 cm at the open pasture and from 38 to 17 cm at the sheltered field, while mean density increased from 0.25–0.28 to 0.40–0.42 g/cm^3. From the relationship between snow properties and relative permittivity, we found that relative permittivity decreased with snow depth but increased with both snow density and LWC, indicating that density and liquid water in the snowpack were the primary controls on the dielectric response in these shallow, wet snowpacks. In the snow density model comparison, the CRIM, Lundberg, and Denoth models, which were developed to represent the dielectric behavior of snow as a mixture of air, ice, and water, showed the closest agreement with GPR-derived permittivity (r = 0.706, 0.706, 0.699, respectively), whereas models calibrated primarily for dry snow or narrowly defined wet-snow regimes underestimated permittivity in these shallow, wet snowpacks. While the modeled values showed reasonable agreement with the GPR-derived permittivity for these shallow, wet snowpacks, it was challenging to distinguish whether observed permittivity changes were driven by changes in snow density or by changes in LWC. Key priorities for future work would therefore be to (1) collect UAS-GPR observations under dry-snow conditions to establish a dielectric baseline, and (2) target periods when snow depth and SWE remain relatively stable but LWC increases, so that permittivity changes associated with wetting can be isolated.

Code and data availability

The datasets generated and analyzed during this study were collected as part of a U.S. Department of Defense-supported research project and are currently subject to sponsor review and approval requirements. As a result, the in situ field observations and associated processing workflows are not presently available in a public repository. The authors are working with the sponsoring agency to determine what data products and code components may

https://doi.org/10.5194/egusphere-2026-3105
Preprint. Discussion started: 28 August 2026

be released during the manuscript review process. Subject to sponsor approval, a subset of the processed datasets and analysis scripts sufficient to reproduce the published results will be made publicly available.

Author contribution

MK: Conceptualization, Formal analysis, Investigation, Visualization, Writing (original draft preparation). AH: Data curation, Software, Writing (review and editing). MM: Investigation, Writing (review and editing). DRG: Methodology, Writing (review and editing). JMJ: Project administration, Supervision, Writing (review and editing).

Competing interests

The authors declare that they have no conflict of interest.

Acknowledgements

The authors thank Jeremy Johnston, Megan Vardaman, Rashik Koirala, and Ryan Reed for their assistance with field sampling and data collection during the winter field campaigns.

Financial support

This material is based upon work supported by the U.S. Department of Defense's Broad Agency Announcement Program and the Cold Regions Research and Engineering Laboratory (ERDC-CRREL) under contract no. BAA3 W913E523C0004 and the National Institute of Food and Agriculture, Agriculture Food and Research Initiative (2021-67019-34345).

References

A2 Photonic Sensors, 2019. WISe - Snow liquid water content sensor - User Manual.

Ajo-Franklin, J.B., Geller, J.T., Harris, J.M., 2004. The dielectric properties of granular media saturated with DNAPL/water mixtures. Geophys. Res. Lett. 31. https://doi.org/10.1029/2004GL020672

Arcone, S. A., Boitnott, G. E., 2012. Maxwell–Wagner relaxation in common minerals and a desert soil at low water contents. J. Appl. Geophy. 81, 97-105.

Artemov, V.G., 2019. A unified mechanism for ice and water electrical conductivity from direct current to terahertz. Physical Chemistry Chemical Physics 21, 8067–8072.

Barnett, T.P., Adam, J.C., Lettenmaier, D.P., 2005. Potential impacts of a warming climate on water availability in snow-dominated regions. Nature 438, 303–309.

Bonnell, R., McGrath, D., Williams, K., Webb, R., Fassnacht, S.R., Marshall, H.-P., 2021. Spatiotemporal variations in liquid water content in a seasonal snowpack: Implications for radar remote sensing. Remote Sens. (Basel). 13, 4223.

Bonnell, R., McGrath, D., Hedrick, A. R., Trujillo, E., Meehan, T. G., Williams, K., Marshall, H.-P., Sexstone, G., Fulton, J., Ronayne, M. J., Fassnacht, S. R., Webb, R. W., Hale, K. E., 2023. Snowpack relative permittivity and density derived from near-coincident lidar and ground-penetrating radar. Hydrol. Process. 37(10), e14996. https://doi.org/10.1002/hyp.14996

Bormann, K.J., Westra, S., Evans, J.P., McCabe, M.F., 2013. Spatial and temporal variability in seasonal snow density. J. Hydrol. (Amst). 484, 63–73. https://doi.org/10.1016/j.jhydrol.2013.01.032

Bradford, J.H., Harper, J.T., Brown, J., 2009. Complex dielectric permittivity measurements from ground-penetrating radar data to estimate snow liquid water content in the pendular regime, Water Resour. Res., 45, W08403, https://doi.org/10.1029/2008WR007341.

Cheng, Y., Cheng, B., Pirazzini, R., Macfarlane, A.R., Vihma, T., Dorn, W., Dadic, R., Schneebeli, M., Arndt, S., Rinke, A., 2025. Seasonal evolution of snow density and its impact on thermal regime of sea ice during the MOSAiC expedition. Cryosphere 19, 6001–6021. https://doi.org/10.5194/tc-19-6001-2025

Cho, E., Verfaillie, M., Jacobs, J.M., Hunsaker, A.G., Sullivan, F.B., Palace, M., Wagner, C., 2025. Characterizing the spatial distribution of field-scale snowpack using unpiloted aerial system (UAS) lidar and structure-from-motion (SfM) photogrammetry. Hydrol. Earth Syst. Sci. 29, 4539–4556.

Denoth, A., 1997. The monopole-antenna: a practical snow and soil wetness sensor. IEEE Transactions on Geoscience and Remote Sensing 35, 1371–1375. https://doi.org/10.1109/36.628804

Endres, A.L., Knight, R., 1992. A THEORETICAL TREATMENT OF THE EFFECT OF MICROSCOPIC FLUID DISTRIBUTION ON THE DIELECTRIC PROPERTIES OF PARTIALLY SATURATED ROCKS 1. Geophys. Prospect. 40, 307–324.

Garcia, A., Glaser, D.R., 2025. Subfreezing complex electrical conductivity hysteresis in frost susceptible soils. Geophys. J. Int. 243, ggaf335.

Glaser, D.R., Barrowes, B.E., Shubitidze, F., Slater, L.D., 2023. Laboratory investigation of high-frequency electromagnetic induction measurements for macro-scale relaxation signatures. Geophys. J. Int. 235, 1274–1291.

Glaser, D.R., Henderson, R.D., Werkema, D.D., Johnson, T.J., Versteeg, R.J., 2022a. Estimating biofuel contaminant concentration from 4D ERT with mixing models. J. Contam. Hydrol. 248, 104027.

Glaser, D.R., Shubitidze, F., Barrowes, B.E., 2022b. Standoff high-frequency electromagnetic induction response of unsaturated sands: A tank-scale feasibility study. J. Environ. Eng. Geophys. 27, 45–51.

Glaser, D.R., Werkema, D.D., Versteeg, R.J., Henderson, R.D., Rucker, D.F., 2012. Temporal GPR imaging of an ethanol release within a laboratory-scaled sand tank. J. Appl. Geophy. 86, 133–145. https://doi.org/10.1016/j.jappgeo.2012.07.016

Hale, K.E., Musselman, K.N., Newman, A.J., Livneh, B., Molotch, N.P., 2023. Effects of snow water storage on hydrologic partitioning across the mountainous, western United States. Water Resour. Res. 59, e2023WR034690.

Harder, P., Pomeroy, J.W., Helgason, W.D., 2020. Improving sub-canopy snow depth mapping with unmanned aerial vehicles: lidar versus structure-from-motion techniques. Cryosphere 14, 1919–1935.

Jennings, K.S., Kittel, T.G.F., Molotch, N.P., 2018. Observations and simulations of the seasonal evolution of snowpack cold content and its relation to snowmelt and the snowpack energy budget. Cryosphere 12, 1595–1614. https://doi.org/10.5194/tc-12-1595-2018

Johnston, J., Jacobs, J.M., Cho, E., 2024. Global Snow Seasonality Regimes from Satellite Records of Snow Cover. J. Hydrometeorol. 25, 65–88. https://doi.org/10.1175/JHM-D-23-0047.1

Judson, A., Doesken, N., 2000. Density of Freshly Fallen Snow in the Central Rocky Mountains. Bull. Am. Meteorol. Soc. 81, 1577–1588. https://doi.org/10.1175/1520-0477(2000)081<1577:DOFFSI>2.3.CO;2

Kendra, J.R., Ulaby, F.T., Sarabandi, K., 1994. Snow probe for in situ determination of wetness and density. IEEE Transactions on Geoscience and Remote Sensing 32, 1152–1159. https://doi.org/10.1109/36.338363

Leão, T.P., Perfect, E., Tyner, J.S., 2015. Evaluation of lichtenecker's mixing model for predicting effective permittivitty of soils at 50 MHZ. Trans. ASABE 58, 83–91. https://doi.org/10.13031/trans.58.10720

Lehning, M., 2013. Snow–atmosphere interactions and hydrological consequences. Adv. Water Resour. 55, 1–3. https://doi.org/10.1016/j.advwatres.2013.02.001

Lundberg, A., Thunehed, H., 2000. Snow wetness influence on impulse radar snow surveys theoretical and laboratory study. Nordic Hydrology 31, 89–106.

Mannello, M.A., Braddock, S., Campbell, S.W., Skelton, E., Schild, K.M., McNeil, C., 2025. Constraining snow water equivalent of wet snowpacks in Southeast Alaska. Ann. Glaciol. 66, e21.

https://doi.org/10.5194/egusphere-2026-3105
Preprint. Discussion started: 28 August 2026

https://doi.org/10.1017/aog.2025.10014

McGrath, D., Bonnell, R., Zeller, L., Olsen-Mikitowicz, A., Bump, E., Webb, R., Marshall, H.-P., 2022. A time series of snow density and snow water equivalent observations derived from the integration of GPR and UAV SfM observations. Frontiers in Remote Sensing 3, 886747.

Mitterer, C., Heilig, A., Schweizer, J., Eisen, O., 2011. Upward-looking ground-penetrating radar for measuring wet-snow properties. Cold Reg. Sci. Technol. 69(2–3), 129–138. https://doi.org/10.1016/j.coldregions.2011.06.003

Pinzer, B.R., Schneebeli, M., 2009. Snow metamorphism under alternating temperature gradients: Morphology and recrystallization in surface snow. Geophys. Res. Lett. 36. https://doi.org/10.1029/2009GL039618

Robinson, D.A., Dewey, K.F., Heim, R.R., 1993. Global Snow Cover Monitoring: An Update. Bull. Am. Meteorol. Soc. 74, 1689–1696. https://doi.org/10.1175/1520-0477(1993)074<1689:GSCMAU>2.0.CO;2

Roth, T.R., Nolin, A.W., 2017. Forest impacts on snow accumulation and ablation across an elevation gradient in a temperate montane environment. Hydrol. Earth Syst. Sci. 21, 5427–5442.

Schön, J.H., 2015. Electrical properties, in: Developments in Petroleum Science. Elsevier, pp. 301–367.

Sihvola, A., Tiuri, M., 1986. Snow Fork for Field Determination of the Density and Wetness Profiles of a Snow Pack. IEEE Transactions on Geoscience and Remote Sensing GE-24, 717–721. https://doi.org/10.1109/TGRS.1986.289619

Simpkin, R., 2010. Derivation of lichtenecker's logarithmic mixture formula from maxwell's equations. IEEE Trans. Microw. Theory Tech. 58, 545–550. https://doi.org/10.1109/TMTT.2010.2040406

Sturm, M., Taras, B., Liston, G.E., Derksen, C., Jonas, T., Lea, J., 2010. Estimating Snow Water Equivalent Using Snow Depth Data and Climate Classes. J. Hydrometeorol. 11, 1380–1394. https://doi.org/10.1175/2010JHM1202.1

Tan, A., Eccleston, K., Platt, I., Woodhead, I., Rack, W., McCulloch, J., 2017. The design of a UAV mounted snow depth radar: Results of measurements on Antarctic sea ice, in: 2017 IEEE Conference on Antenna Measurements & Applications (CAMA). pp. 316–319. https://doi.org/10.1109/CAMA.2017.8273437

Thackeray, C.W., Qu, X., Hall, A., 2018. Why do models produce spread in snow albedo feedback? Geophys. Res. Lett. 45, 6223–6231.

Tiuri, M., Sihvola, A., Nyfors, E., Hallikainen, M.T., 1984. The complex dielectric constant of snow at microwave frequencies. IEEE J. Ocean. Eng. 9(5), 377–382. https://doi.org/10.1109/JOE.1984.1145645

Valence, E., Baraer, M., Rosa, E., Barbecot, F., Monty, C., 2022. Drone-based ground-penetrating radar (GPR) application to snow hydrology. Cryosphere 16, 3843–3860.

Verfaillie, M., Cho, E., Dwyre, L., Khan, I., Wagner, C., Jacobs, J.M., Hunsaker, A., 2023. UAS remote sensing applications to abrupt cold region hazards. Front. Remote Sens. 4, 1095275. https://doi.org/10.3389/frsen.2023.1095275

von Hippel, A.R., Morgan, S.O., 1955. Dielectric Materials and Applications. J. Electrochem. Soc. 102, 68Ca. https://doi.org/10.1149/1.2430014

Webb, R.W., Jennings, K.S., Fend, M., Molotch, N.P., 2018. Combining ground-penetrating radar with terrestrial LiDAR scanning to estimate the spatial distribution of liquid water content in seasonal snowpacks. Water Resour. Res. 54, 10339–10349. https://doi.org/10.1029/2018WR022680

Webb, R.W., Marziliano, A., McGrath, D., Bonnell, R., Meehan, T.G., Vuyovich, C., Marshall, H.P., 2021. In situ determination of dry and wet snow permittivity: Improving equations for low frequency radar applications. Remote Sens. (Basel). 13. https://doi.org/10.3390/rs13224617

Whitehead, K., Hugenholtz, C.H., Myshak, S., Brown, O., LeClair, A., Tamminga, A., Barchyn, T.E., Moorman, B., Eaton, B., 2014. Remote sensing of the environment with small unmanned aircraft systems (UASs), part 2: scientific and commercial applications. J. Unmanned Veh. Syst. 2, 86–102.

Wilhelms, F., 2005. Explaining the dielectric properties of firn as a density-and-conductivity mixed permittivity (DECOMP). Geophys. Res. Lett., 32, L16501. https://doi.org/10.1029/2005GL022808

Zhao, W., Mu, C., Han, L., Sun, W., Sun, Y., Zhang, T., 2023. Spatial and temporal variability in snow density across the Northern Hemisphere. Catena (Amst). 232, 107445.

https://doi.org/10.5194/egusphere-2026-3105
Preprint. Discussion started: 28 August 2026

https://doi.org/10.1016/j.catena.2023.107445